Biomechanics and Modeling in Mechanobiology
https://doi.org/10.1007/s10237-019-01184-8

ORIGINAL PAPER

Patient-specific predictions of aneurysm growth and remodeling in the ascending thoracic aorta using the homogenized constrained mixture model

S. Jamaleddin Mousavi[1] · **Solmaz Farzaneh**[1] · **Stéphane Avril**[1]

Received: 15 January 2019 / Accepted: 5 June 2019

Abstract
In its permanent quest of mechanobiological homeostasis, our vasculature significantly adapts across multiple length and timescales in various physiological and pathological conditions. Computational modeling of vascular growth and remodeling (G&R) has significantly improved our insights into the mechanobiological processes of diseases such as hypertension or aneurysms. However, patient-specific computational modeling of ascending thoracic aortic aneurysm (ATAA) evolution, based on finite element models (FEM), remains a challenging scientific problem with rare contributions, despite the major significance of this topic of research. Challenges are related to complex boundary conditions and geometries combined with layer-specific G&R responses. To address these challenges, in the current paper, we employed the constrained mixture model (CMM) to model the arterial wall as a mixture of different constituents such as elastin, collagen fiber families and smooth muscle cells. Implemented in Abaqus as a UMAT, this first patient-specific CMM-based FEM of G&R in human ATAA was first validated for canonical problems such as single-layer thick-wall cylindrical and bilayer thick-wall toric arterial geometries. Then it was used to predict ATAA evolution for a patient-specific aortic geometry, showing that the typical shape of an ATAA can be simply produced by elastin proteolysis localized in regions of deranged hemodymanics. The results indicate a transfer of stress to the adventitia by elastin loss and continuous adaptation of the stress distribution due to change in ATAA shape. Moreover, stress redistribution leads to collagen deposition where the maximum elastin mass is lost, which in turn leads to stiffening of the arterial wall. As future work, the predictions of this G&R framework will be validated on datasets of patient-specific ATAA geometries followed up over a significant number of years.

Keywords Finite elements · Constrained mixture theory · Growth and remodeling · Anisotropic behavior · Zero-pressure configuration · Residual stresses

List of symbols

$\mathbf{a}_0^k$	The unit vector pointing direction of the kth fiber
$\mathbf{C}_{\mathrm{el}}^i$	Elastic right Cauchy–Green deformation tensor of the ith constituent
$\overline{\mathbf{C}}_{\mathrm{el}}^i$	Modified elastic right Cauchy–Green deformation tensor of the ith constituent
$D_{\max}$	Maximum damage of elastin
$\dot{D}_{\mathrm{g}}^i$	Generic rate function of ith constituent
$\mathbf{F}$	Total deformation gradient of the mixture
$\mathbf{F}_{\mathrm{tot}}^i$	Total deformation gradient of the ith constituent
$\mathbf{F}_{\mathrm{el}}^i$	Elastic deformation gradient of the ith constituent
$\mathbf{F}_{\mathrm{gr}}^i$	Total inelastic (G&R) deformation gradient of the ith constituent
$\mathbf{F}_{\mathrm{g}}^i$	Deformation gradient of the ith constituent due to growth
$\mathbf{F}_{\mathrm{r}}^i$	Deformation gradient of the ith constituent due to remodeling
$\mathbf{G}_{\mathrm{h}}^i$	Deposition stretch tensor of the ith constituent
J	Jacobian of the mixture
$\overline{I}_1^i$	First invariant of the right Cauchy–Green deformation tensor for the ith constituent
I_4^i	Fourth invariant of the right Cauchy–Green deformation tensor for the ith constituent

In the list of symbols, $i \in \{\mathrm{e}, \mathrm{c}_j, \mathrm{m}\}$ and $k \in \{\mathrm{c}_j, \mathrm{m}\}$

✉ Stéphane Avril
Avril@emse.fr

[1] Mines Saint-Étienne, INSERM, U 1059 Sainbiose, Centre CIS, University of Lyon, Université Jean Monnet, 42023 Saint-Étienne, France

Published online: 14 June 2019

$k_{\sigma}^{c_j}$	Gain or growth parameter of collagen fiber families
k_1^k	Fung-type material coefficient the kth constituent
k_2^k	Fung-type material coefficient the kth constituent
L_{dam}	Spatial damage spread parameter of elastin
$\mathbf{S}$	Second Piola–Kirchhoff stress
T^i	Average turnover time of the ith constituent
t_{dam}	Temporal damage spread parameter of elastin
W	The specific strain energy density function of the mixture
W^i	Strain energy of the ith individual constituents
$\mathbf{X}$	Material point in a reference configuration
$\mathbf{x}$	Material point in a deformed or current configuration
α^{c_j}	Each direction of collagen fiber families
μ^{e}	Neo-Hookean material coefficient of elastin
κ	Bulk modulus of elastin
σ^i	Current stress of extant ith constituent
$\sigma_{\text{h}}^{c_j}$	Average stress of ith constituent at homeostasis
λ_z^{e}	Axial elastin deposition stretch value
$\lambda_\theta^{\text{e}}$	Circumferential elastin deposition stretch value
λ^k	Deposition stretch value of kth constituent in fiber direction
$\mathbf{\Omega}_0$	Reference configuration
$\mathbf{\Omega}(t)$	Deformed or current configuration
ϱ_0^i	Mass densities of the ith constituent before G&R
ϱ_t^i	Mass densities of the ith constituent at time t
$\dot{\varrho}^{\text{e}}(t)$	Rate of mass degradation of the elastin
$\dot{\varrho}_{\text{adv}}^{c_j}(t)$	Rate of mass degradation or deposition in the adventitia for collagen fibers
$\dot{\varrho}_{\text{med}}^{c_j}(t)$	Rate of mass degradation or deposition in the media for collagen fibers

1 Introduction

Growth and remodeling (G&R) are fundamental mechano-biological processes in normal tissue development and in various pathological conditions. It is suggested that G&R in tissues may be mediated by mechanical stresses. For example, cardiac hypertrophy and normal cardiac growth develop in response to increased hemodynamic loading and altered systolic and diastolic wall stresses (Grossman 1980). Sustained hypertension is also associated with changes such as increased wall thickness in large arteries (Humphrey 2008a). This adaptation ability of soft tissues is related to the existence of a mechanical homeostasis across multiple length and timescales in the vasculature. At the tissue scale, this manifests through continuous mass changes in the components of the extracellular matrix (ECM) such as collagen, elastin and proteoglycans (Cyron et al. 2016; Humphrey and Rajagopal 2002).

In the current paper, we are interested in continuum finite element formulations to simulate G&R in arteries. The first model of mechanoregulated soft tissue growth was presented by Rodriguez and Hoger (1994) in the mid-1990s, incorporating the associated growth by multiplicative decomposition of the total deformation gradient into an elastic and inelastic part. Thereafter, this conceptual simplicity has been widely used by others. Comellas et al. (2016) introduced an original constitutive model to study remodeling of damaged tissue within the framework of continuum damage mechanics and open-system thermodynamics. The total damage rate was calculated as the sum of a healing rate and a mechanical damage rate. In order to couple biochemical and biomechanical damage, the healing rate was driven by mechanical stimuli and subjected to simple metabolic constraints. Although their model was based on the mixture theory, it did not account for the evolving prestretch of each constituent.

Although many theories of G&R have modeled the tissue as a homogenized (single-constituent) solid continuum (Hosseini et al. 2017; Hosseini and Taber 2018), the constrained mixture model (CMM) has been increasingly employed by a number of authors (Baek et al. 2006; Braeu et al. 2017; Cyron et al. 2016; Famaey et al. 2018; Figueroa et al. 2009; Latorre and Humphrey 2018a; Lin et al. 2017; Valentín and Holzapfel 2012; Valentín et al. 2013; Watton et al. 2004; Zeinali-Davarani and Baek 2012) to simulate G&R in arteries, including non-homogenized (Famaey et al. 2018; Valentín and Holzapfel 2012; Valentín et al. 2013) and homogenized (Braeu et al. 2017; Cyron et al. 2016; Lin et al. 2017) approaches. For example, Valentín et al. (2013, 2011) established a nonlinear finite element model (FEM) based on the non-homogenized constrained mixture theory (CMT) of G&R to facilitate numerical analyses of various cases of arterial adaptation and maladaptation. Watton et al. (2004) presented the first mathematical framework to study G&R in two-layered cylindrical membranes. In their framework, the natural configurations of each individual constituent were updated at each time step, and thus, cell-mediated G&R effects could be handled (Humphrey and Holzapfel 2012). They introduced collagen fiber recruitment and collagen fibre density in the strain energy density functions. Baek et al. (2006) made another important contribution to study the growth of intracranial cerebral aneurysms with a constrained mixture thin-walled model, permitting to account for evolving strain energy density functions. Although both adopted a CMM (deforming different constituents altogether under a total mixture deformation gradient but having different natural reference configurations), the mathematical foundations were slightly different. The former employed a rate-based approach, while the latter used an integral approach. The rate-based approach was shown to be more efficient and as accurate as the integral one (Gasser and

Grytsan 2017). Including disease progression and evolving geometries, CMT-based models were able to predict changes in fiber orientations and quantities, degradation of elastin and loss of smooth muscle cells (SMCs). The same concept was implemented by Famaey et al. (2018) in Abaqus (Hibbit and Sorensen 2011) to predict adaptation of a pulmonary autograft over an extended period. There are a number of other applied contributions considering, for example:

- two-dimensional (2D) non-homogenized CMM for arterial G&R proposed by Baek et al. (2006), for cerebral aneurysms and extended by Valentín et al. (2009), Valentín and Humphrey (2009a) and Valentín and Humphrey (2009b) for cerebral arteries
- the evolving geometry, structure and mechanical properties of a representative straight cylindrical artery subjected to changes in mean blood pressure and flow in 3D (Karšaj et al. 2010).

Braeu et al. (2017) and Cyron et al. (2016) introduced the homogenized CMM framework for G&R using an informal temporal averaging approach. Lin et al. (2017) combined homogenization and the CMT to simulate the dilatation of abdominal aortic aneurysms. Their methodology is computationally less expensive than non-homogenized CMM and it can yet capture important aspects of G&R such as mass turnover in arterial walls. Unlike non-homogenized CMMs in which one must deal with myriads of evolving configurations, the homogenized CMM is based on a single time-independent reference configuration for each material species and each point with a time-dependent inelastic local deformation of G&R. Recently, Latorre and Humphrey (2018b) have introduced a new rate-based CMM formulation suitable for studying mechanobiological equilibrium and stability of soft tissues exposed to transient or sustained changes, permitting direct resolution of G&R problems with a static approach.

Although prior work on the CMM framework has significantly improved our insights into arterial wall G&R, they have been mostly limited to canonical problems in arterial mechanics such as 2D (Baek et al. 2006; Valentín et al. 2009; Valentín and Humphrey 2009a, b) or simplified 3D cases, using membrane (Cyron et al. 2016) or single-layer thick-wall axisymmetric (Braeu et al. 2017; Lin et al. 2017) approximations. Therefore, the framework still requires to be extended to more realistic and diverse analyses including patient-specific arterial geometries. To this end, several problems still need to be addressed within the CMM framework such as layer specificity, irregular boundary conditions and complex deformations. These problems can become extremely challenging in the case of ascending thoracic aortic aneurysms (ATAA) due to the simultaneous and region-specific evolution of geometry, material properties (Farzaneh et al. 2018) and hemodynamic loads (Condemi et al. 2017; Humphrey and Holzapfel 2012).

In the present work, the objective is to set up the first nonlinear FEM based on the homogenized CMT to simulate G&R in patient-specific ATAA. After its implementation, the FEM is first validated on an idealized single-layer thick-wall cylinder. In a second stage, the model is illustrated for a canonical problem in arterial mechanics: G&R of a toric bilayer thick-wall arterial geometry. Then it is used to predict ATAA evolution for a patient-specific aortic geometry, showing that the typical shape of an ATAA can be obtained simply with a proteolysis of elastin localized in regions of deranged hemodymanics.

2 Material and methods

2.1 G&R kinematics

Let $\chi : \mathbf{\Omega}_0$ be the general mapping in a $\mathbb{R}^3$ domain. $\mathbf{\Omega}_0$ is considered as the in vivo (for example, healthy) configuration of a blood vessel before any specific G&R starts. The total deformation gradient of a mixture of n different constituents (e.g., elastin, collagen fiber families or SMCs), $\mathbf{F}$, between a material point, $\mathbf{X} \in \mathbf{\Omega}_0$, from a reference configuration, $\mathbf{\Omega}(0) = \mathbf{\Omega}_0$, and a position, $\mathbf{x} = \chi(\mathbf{X}, t) \in \mathbf{\Omega}_0$, in a deformed or current configuration, $\mathbf{\Omega}(t) = \mathbf{\Omega}_t$, at time t can be defined as

$$\mathbf{F}(\mathbf{X}, t) = \frac{\partial \mathbf{x}}{\partial \mathbf{X}} \tag{1}$$

Reference volume elements $\mathrm{d}V \in \mathbf{\Omega}_0$ are mapped to volume elements $\mathrm{d}v = J\mathrm{d}V \in \mathbf{\Omega}_t$ with the Jacobian $J = \mid \mathbf{F} \mid > 0$.

According to the CMT, we assume that all constituents in the mixture deform together under the total deformation gradient $\mathbf{F}$ in the stressed field, while each constituent has a different "total" deformation gradient resulting from its own deposition stretch. Therefore, assuming that $\mathbf{G}^i_{\mathrm{h}}$ ($i \in \{\mathrm{e}, \mathrm{c}_j, \mathrm{m}\}$, where superscripts e, c_j and m represent, respectively, the elastin, the constituent made of each of the n possible collagen fiber families and the SMCs, all these constituents making the mixture) is the initial deposition stretch of the ith constituent with respect to the reference homeostatic configuration (Cardamone et al. 2009; Mousavi and Avril 2017; Mousavi et al. 2018), the "total" deformation gradient of the ith constituent can be calculated as

$$\mathbf{F}^i_{\mathrm{tot}} = \mathbf{F}\mathbf{G}^i_{\mathrm{h}} \tag{2}$$

where the initial deposition stretch tensor of elastin may be written as $\mathbf{G}^{\mathrm{e}}_{\mathrm{h}} = \mathrm{diag}[\frac{1}{\lambda^{\mathrm{e}}_{\theta}\lambda^{\mathrm{e}}_{z}}, \lambda^{\mathrm{e}}_{\theta}, \lambda^{\mathrm{e}}_{z}]$ to ensure incompressibility, and the initial deposition stretch tensor of collagen families and

SMCs may be written as $\mathbf{G}_{\mathrm{h}}^{\mathrm{k}} = \lambda^k \mathbf{a}_0^k \otimes \mathbf{a}_0^k + \frac{1}{\sqrt{\lambda^k}}(\mathbf{I} - \mathbf{a}_0^k \otimes \mathbf{a}_0^k)$, $k \in \{\mathrm{c}_j, \mathrm{m}\}$. $\lambda_\theta^{\mathrm{e}}$ and λ_z^{e} are the initial deposition stretches of elastin in the circumferential and longitudinal directions, respectively, and λ^k is the initial deposition stretch of the kth constituent in the reference fiber direction with a unit vector $\mathbf{a}_0^k$.

The local stress-free state may vary between each constituent and even with time. Thus, for each differential mass increment of the ith constituent deposited at time τ, the total deformation gradient of each constituent in Eq. 2 may be rewritten by a multiplicative decomposition into an elastic $\mathbf{F}_{\mathrm{el}}^i$ and inelastic (namely G&R) part $\mathbf{F}_{\mathrm{gr}}^i$ as

$$\mathbf{F}_{\mathrm{tot}}^i = \mathbf{F}_{\mathrm{el}}^i \mathbf{F}_{\mathrm{gr}}^i \tag{3}$$

It is noteworthy that due to continuous G&R, the inelastic G&R deformation gradient includes the changes between the local stress-free configurations of different mass increments resulting from deposition in a different configuration and at a different time. This process is schematically shown in Fig. 1. Dynamic effects such as inertia or viscoelasticity can usually be neglected during G&R as they occur at slow timescales (Braeu et al. 2017).

2.2 Mechanical constitutive model of arterial wall

Numerous mechanical constitutive models were introduced for arterial walls (Holzapfel et al. 2000). In this section, a strain energy density function is defined for the different components of the arterial wall based on the CMT (Braeu et al. 2017; Cyron et al. 2014, 2016; Mousavi and Avril 2017; Mousavi et al. 2018; Wilson et al. 2013). These different components are: elastin, four different families of collagen fibers oriented in circumferential, axial and diagonal directions and SMCs. The intima layer is disregarded here as it is very thin. Based on the mass fractions of each individual component, the specific

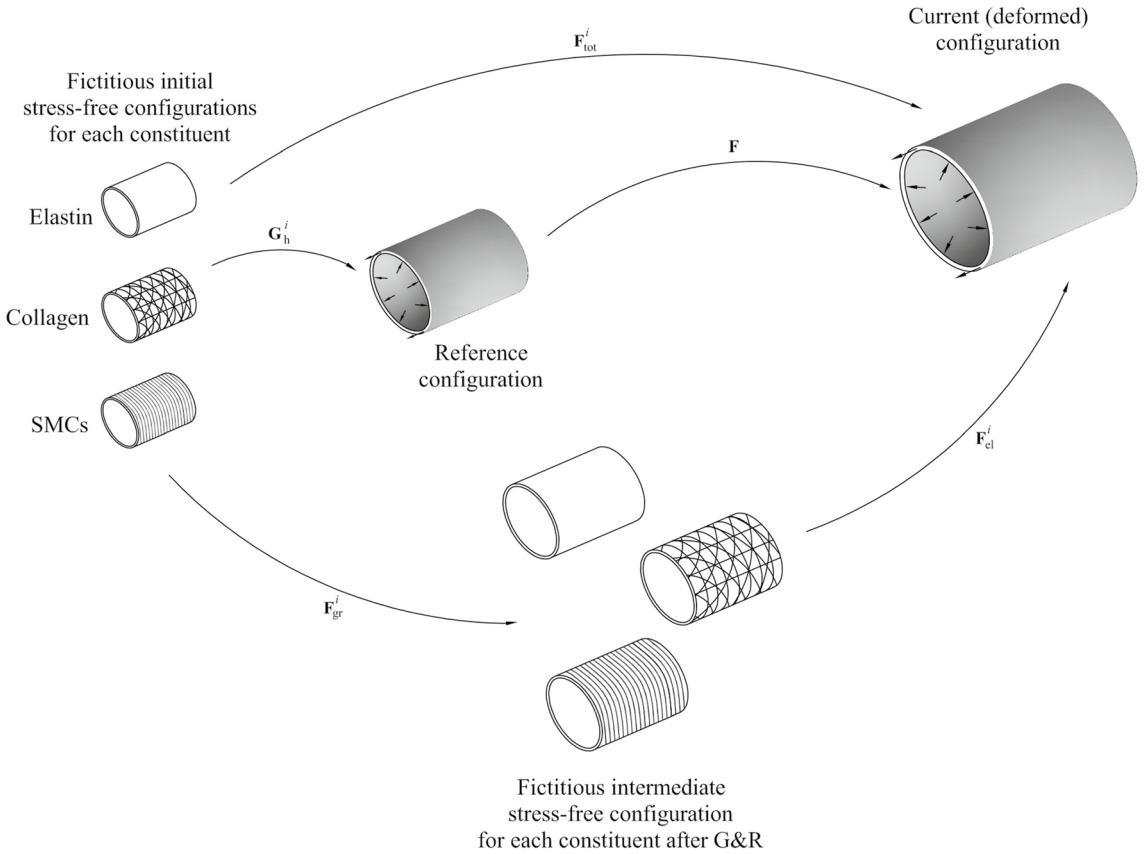

Fig. 1 A body in a reference configuration is assumed to be a mixture of different constituents whose stress-free initial configuration is related to the reference configuration by the initial deposition stretch tensor $\mathbf{G}_{\mathrm{h}}^i$. From the reference configuration to the current configuration, the body undergoes a deformation gradient denoted $\mathbf{F}$. From their respective initial fictitious stress-free configuration to the current configuration, each constituent undergoes a total deformation $\mathbf{F}_{\mathrm{tot}}^i$ which can be decomposed multiplicatively into an elastic part $\mathbf{F}_{\mathrm{el}}^i$ and an inelastic part $\mathbf{F}_{\mathrm{gr}}^i$. The latter is caused by growth and remodeling and leads to a stress-free fictitious intermediate configuration for each constituent

strain energy density function may be written as Braeu et al. (2017), Humphrey (1995), Mousavi and Avril (2017) and Mousavi et al. (2018):

$$W = \varrho_t^{\mathrm{e}}\left(\overline{W}^{\mathrm{e}}(\overline{I}_1^{\mathrm{e}}) + U(J_{\mathrm{el}}^{\mathrm{e}})\right) + \sum_{j=1}^{n} \varrho_t^{\mathrm{c}_j} W^{\mathrm{c}_j}(I_4^{\mathrm{c}_j}) + \varrho_t^{\mathrm{m}} W^{\mathrm{m}}(I_4^{\mathrm{m}}) \tag{4}$$

where ϱ_t^i and W^i ($i \in \{\mathrm{c}_j, \mathrm{m}\}$) refer, respectively, to the mass densities and strain energy of the individual constituents based on the first ($\overline{I}_1^i$), fourth (I_4^i) invariants and Jacobian (J).

Strain energy density of elastin is described by a neo-Hookean function in which incompressibility is enforced by a penalty function of the Jacobian (Cardamone et al. 2009; Holzapfel et al. 2000; Mousavi and Avril 2017) as

$$\overline{W}^{\mathrm{e}}(\overline{I}_1^{\mathrm{e}}) = \frac{\mu^{\mathrm{e}}}{2}(\overline{I}_1^{\mathrm{e}} - 3) \tag{5a}$$

$$U^{\mathrm{e}}(J_{\mathrm{el}}^{\mathrm{e}}) = \kappa(J_{\mathrm{el}}^{\mathrm{e}} - 1)^2 \tag{5b}$$

where μ^{e} and κ are, respectively, a material parameter and the bulk modulus (stress-like dimensions), and

$$\overline{I}_1^{\mathrm{e}} = tr(\overline{\mathbf{C}}_{\mathrm{el}}^{\mathrm{e}}) \tag{6a}$$

$$\overline{\mathbf{C}}_{\mathrm{el}}^{\mathrm{e}} = \overline{\mathbf{F}}_{\mathrm{el}}^{\mathrm{e}\,(\mathrm{T})}\overline{\mathbf{F}}_{\mathrm{el}}^{\mathrm{e}} \tag{6b}$$

$$\overline{\mathbf{F}}_{\mathrm{el}}^{\mathrm{e}} = \frac{1}{J_{\mathrm{el}}^{\mathrm{e}\,1/3}}\mathbf{F}_{\mathrm{el}}^{\mathrm{e}} \tag{6c}$$

$$J_{\mathrm{el}}^{\mathrm{e}} = \det(\mathbf{F}_{\mathrm{el}}^{\mathrm{e}}) > 0 \tag{6d}$$

Note that $\det(\overline{\mathbf{F}}_{\mathrm{el}}^{\mathrm{e}}) = 1$.

The passive strain energy density of collagen families and SMCs are described using an exponential expression, respectively, as (Cardamone et al. 2009; Mousavi and Avril 2017; Riveros et al. 2013; Rodriguez et al. 2008)

$$W^{\mathrm{c}_j}(I_4^{\mathrm{c}_j}) = \frac{k_1^{\mathrm{c}_j}}{2k_2^{\mathrm{c}_j}}\left[\mathrm{e}^{k_2^{\mathrm{c}_j}(I_4^{\mathrm{c}_j}-1)^2} - 1\right] \tag{7}$$

and

$$W^{\mathrm{m}}(I_4^{\mathrm{m}}) = \frac{k_1^{\mathrm{m}}}{2k_2^{\mathrm{m}}}\left[\mathrm{e}^{k_2^{\mathrm{m}}(I_4^{\mathrm{m}}-1)^2} - 1\right] \tag{8}$$

$k_1^{\mathrm{c}_j}$ and k_1^{m} are stress-like material parameters, while $k_2^{\mathrm{c}_j}$ and k_2^{m} are dimensionless material parameters. These parameters can take different values when fibers are under compression or tension (Bersi et al. 2016; Mousavi et al. 2018). Note that the fourth invariant and right Cauchy–Green stretch tensor can, respectively, be written as

$$I_4^k = \frac{1}{\|F_{gr}\mathbf{a}_0^k\|^2}\mathbf{C}_{\mathrm{el}}^k : (\mathbf{F}_{\mathrm{gr}}^k\mathbf{a}_0^k) \otimes (\mathbf{F}_{\mathrm{gr}}^k\mathbf{a}_0^k) = \frac{1}{\|F_{gr}\mathbf{a}_0^k\|^2}\mathbf{C}_{\mathrm{tot}}^k : \mathbf{a}_0^k \otimes \mathbf{a}_0^k \tag{9a}$$

$$\mathbf{C}_{\mathrm{tot/el}}^k = (\mathbf{F}_{\mathrm{tot/el}}^k)^T\mathbf{F}_{\mathrm{tot/el}}^k \tag{9b}$$

where $k \in \{\mathrm{c}_j, \mathrm{m}\}$.

For every 3D hexahedral or tetrahedral finite element across the geometry of the artery, the same strain energy density function is assumed; however, different material properties and mass densities of the individual constituents may be used for each layer (media and adventitia).

Referring to Eq. 4 leads to the expression of the second Piola–Kirchhoff stress tensor as:

$$\begin{aligned}\mathbf{S} = {} & \varrho_t^{\mathrm{e}}[J_{\mathrm{el}}^{\mathrm{e}\,-2/3}\mu^{\mathrm{e}}(\mathbf{I} - 1/3J_{\mathrm{el}}^{\mathrm{e}}\mathrm{Tr}(\mathbf{F}_{\mathrm{el}}^{\mathrm{e}}\mathbf{F}_{\mathrm{el}}^{\mathrm{e}\,T})\mathbf{C}_{\mathrm{el}}^{\mathrm{e}\,-1}) + J_{\mathrm{el}}^{\mathrm{e}}p\mathbf{C}_{\mathrm{el}}^{\mathrm{e}\,-1}] \\ & + 2\sum_{j=1}^{n}\frac{\varrho_t^{\mathrm{c}_j}}{\|F_{gr}\mathbf{a}_0^k\|^2}\frac{\partial W^{\mathrm{c}_j}}{\partial I_4^{\mathrm{c}_j}}(\mathbf{F}_{\mathrm{gr}}^{\mathrm{c}_j}\mathbf{a}_0^{\mathrm{c}_j}) \otimes (\mathbf{F}_{\mathrm{gr}}^{\mathrm{c}_j}\mathbf{a}_0^{\mathrm{c}_j}) \\ & + 2\frac{\varrho_t^{\mathrm{m}}}{\|F_{gr}\mathbf{a}_0^k\|^2}\frac{\partial W^{\mathrm{m}}}{\partial I_4^{\mathrm{m}}}(\mathbf{F}_{\mathrm{gr}}^k\mathbf{a}_0^m) \otimes (\mathbf{F}_{\mathrm{gr}}^k\mathbf{a}_0^m)\end{aligned} \tag{10}$$

where $p = \frac{\mathrm{d}U^{\mathrm{e}}}{\mathrm{d}J_{\mathrm{el}}^{\mathrm{e}}}$, is the hydrostatic pressure per unit mass. The Cauchy stress tensor is derived from the second Piola–Kirchhoff stress as

$$\begin{aligned}\boldsymbol{\sigma} = {} & \varrho_t^{\mathrm{e}}(J_{\mathrm{el}}^{\mathrm{e}\,-5/3}\mu^{\mathrm{e}}(\mathbf{F}_{\mathrm{el}}^{\mathrm{e}}\mathbf{F}_{\mathrm{el}}^{\mathrm{e}\,T} - 1/3\mathrm{Tr}(\mathbf{F}_{\mathrm{el}}^{\mathrm{e}}\mathbf{F}_{\mathrm{el}}^{\mathrm{e}\,T})\mathbf{I}) + p\mathbf{I}) \\ & + 2\sum_{j=1}^{n}\frac{\varrho_t^{\mathrm{c}_j}}{\|F_{gr}\mathbf{a}_0^k\|^2}\frac{\partial W^{\mathrm{c}_j}}{\partial I_4^{\mathrm{c}_j}}(\mathbf{F}_{\mathrm{tot}}^{\mathrm{c}_j}\mathbf{a}_0^{\mathrm{c}_j}) \otimes (\mathbf{F}_{\mathrm{tot}}^{\mathrm{c}_j}\mathbf{a}_0^{\mathrm{c}_j}) \\ & + 2\frac{\varrho_t^{\mathrm{m}}}{\|F_{gr}\mathbf{a}_0^k\|^2}\frac{\partial W^{\mathrm{m}}}{\partial I_4^{\mathrm{m}}}(\mathbf{F}_{\mathrm{tot}}^k\mathbf{a}_0^m) \otimes (\mathbf{F}_{\mathrm{tot}}^k\mathbf{a}_0^m)\end{aligned} \tag{11}$$

2.2.1 Mass turnover and inelastic G&R deformation gradient

In CMT-based models, G&R is a conceptual phenomenon during which simultaneous degradation and deposition of different constituents continuously occur. This mass turnover is a stress-mediated process during which extant mass is continuously degraded and new mass is deposited into the extant matrix by a stress-mediated rate (Braeu et al. 2017; Cyron et al. 2016; Famaey et al. 2018). In this work, in two-layer arterial models, mass turnover of collagen families is mediated by SMC stresses in the media and by collagen stresses in the adventitia. (For the latter, it is assumed that fibroblasts of the adventitia would be sensitive to the stresses of collagen, in both intensity and directionality.) Therefore,

the rate of mass degradation or deposition in the media and in the adventitia can be, respectively, calculated as

$$\dot{\varrho}^{c_j}_{\text{med}}(t) = \varrho^{c_j}_t k^{c_j}_\sigma \frac{\sigma^{\text{m}} - \sigma^{\text{m}}_{\text{h}}}{\sigma^{\text{m}}_{\text{h}}} + \dot{D}^{c_j}_{\text{g}} \tag{12a}$$

$$\dot{\varrho}^{c_j}_{\text{adv}}(t) = \varrho^{c_j}_t k^{c_j}_\sigma \frac{\sigma^{c_j} - \sigma^{c_j}_{\text{h}}}{\sigma^{c_j}_{\text{h}}} + \dot{D}^{c_j}_{\text{g}} \tag{12b}$$

where $\varrho^{c_j}_t = \varrho^{c_j}(t)$ are mass densities of collagen families at time t, $k^{c_j}_\sigma$ stands for collagen growth (gain) parameter, $\sigma^{\text{m}}_{\text{h}}$ and $\sigma^{c_j}_{\text{h}}$ are average SMCs and collagen fiber stresses at homeostasis, and σ^{m} and σ^{c_j} denote the current stress of extant collagen fibers and SMCs.

Moreover, it is assumed that elastin can be only subjected to degradation, if any, and its mass loss cannot be compensated by new elastin deposition.

$$\dot{\varrho}^{\text{e}}(t) = \dot{D}^{\text{e}}_{\text{g}} \tag{13}$$

$\dot{D}^{c_j}_{\text{g}}$ and $\dot{D}^{\text{e}}_{\text{g}}$, the so-called generic rate function, is used to describe additional deposition or degradation due to any damage in collagen and elastin, respectively. Those are not stress-mediated but can be driven by other factors like chemical degradation processes or mechanical fatigue. Besides, no mass turnover is assumed for SMCs.

Even when there is a mass balance between mass degradation and mass production ($\dot{\varrho}^i_t = 0$), the traction-free state changes as new mass is deposited with a prestress which is not usually identical to the current stress at which the existing mass is removed. This results in changes in the current average stress and, in turn, of the traction-free state of a constituent. Therefore, some change in the microstructure of the tissue, the so-called remodeling, should accompany this mass balance. However, the local traction-free configuration of a constituent will be changed also by growth when there is no mass balance between mass degradation and production ($\dot{\varrho}^i_t \neq 0$). Thus, in addition to this turnover-based remodeling, which is a volume preserving process, the mass turnover is generally associated with a local change in the volume by growth which accommodates the mass in a certain region of the body. Consequently, the traction-free configuration of a certain constituent should be amended by both remodeling- and growth-related inelastic local changes in the microstructure and volume. To this end, we take advantage of the homogenized CMT-based G&R model presented by Braeu et al. (2017) and Cyron et al. (2016). Therefore, multiplicative decomposition of the inelastic G&R deformation gradient of the ith constituent deposited at different times reads

$$\mathbf{F}^i_{\text{gr}} = \mathbf{F}^i_{\text{r}} \mathbf{F}^i_{\text{g}} \tag{14}$$

where $\mathbf{F}^i_{\text{g}}$ and $\mathbf{F}^i_{\text{r}}$ are inelastic deformation gradients due to G&R, respectively. The former is related to any change in the mass per unit reference volume and the latter captures changes in the average deposition stretch tensor due to deposition of new fibers. Therefore, having the net mass production rate based on Braeu et al. (2017) and Cyron et al. (2016), the evolution of the inelastic remodeling deformation gradient of the ith constituent at time t is calculated by solving the following system of equations

$$\left[\frac{\dot{\varrho}^i_t}{\varrho^i_t} + \frac{1}{T^i}\right]\left[\mathbf{S}^i - \mathbf{S}^i_{\text{pre}}\right] = \left[2\frac{\partial \mathbf{S}^i}{\partial \mathbf{C}^i_{\text{el}}} : (\mathbf{C}^i_{\text{el}} \mathbf{L}^i_{\text{r}})\right] \tag{15}$$

where $\mathbf{S}$ is the second Piola–Kirchhoff stress and subscript "pre" denotes deposition prestress, while $\mathbf{L}^i_{\text{r}} = \dot{\mathbf{F}}^i_{\text{r}} \mathbf{F}^{i\,-1}_{\text{r}}$ is the remodeling velocity gradient. T^i is the period within which a mass increment is degraded and replaced by a new mass increment, named the average turnover time.

It is assumed that elastin is not produced any longer during adulthood; it even undergoes a slow degradation with a half-life time of several decades (Braeu et al. 2017; Cyron and Humphrey 2016). Therefore, elastin growth can be basically calculated based on its degradation rate ($\dot{D}^{\text{e}}_{\text{g}}$) which in turn depends on elastin half-life time (some decades). This implies that the remodeling velocity gradient is zero; then, the remodeling gradient is the identity ($\mathbf{L}^{\text{e}}_{\text{r}} = \mathbf{0}$, $\dot{\mathbf{F}}^{\text{e}}_{\text{r}} = \mathbf{0}$ and $\mathbf{F}^{\text{e}}_{\text{r}} = \mathbf{I}$).

Any change in the mass of each constituent in a region of the arterial wall generally induces a local change in wall volume which can be captured by an inelastic deformation gradient, namely the growth deformation gradient. The inelastic growth deformation gradient relates the change in shape and size of a differential volume element to the degraded or deposited mass in that element. Basically it is the geometrical and micromechanical features of the underlying growth process that dictates the local deformation gradient due to a certain mass change. The degradation or deposition of each constituent induces element deformations at each time increment that can be captured by an inelastic deformation gradient rate for each constituent. Based on the homogenized CMT, Braeu et al. (2017) suggested that all constituents experience the same inelastic growth deformation gradient: $\mathbf{F}^i_{\text{g}} = \mathbf{F}_{\text{g}}$. Therefore, the total inelastic growth deformation gradient rate equals the sum of the growth-related deformation gradient rates of each individual constituent and can be obtained by

$$\dot{\mathbf{F}}_{\text{g}} = \sum_{i=1}^{n} \frac{\dot{\varrho}^i_t}{\varrho^{\text{tot}}_t \left[\mathbf{F}^{i\,-\text{T}}_{\text{g}} : \mathbf{a}^i_{\text{g}} \otimes \mathbf{a}^i_{\text{g}}\right]} \mathbf{a}^i_{\text{g}} \otimes \mathbf{a}^i_{\text{g}} \tag{16}$$

where unit vector $\mathbf{a}_g^i$ stands for growth direction of individual constituents which, for example, can represent an anisotropic growth in arterial wall thickness direction. $\varrho_t^{\text{tot}} = \sum_{i=1}^{n} \varrho_t^i$ denotes total volumic mass at each time. It is noteworthy that SMCs do not experience growth according to Eq. 16, which means that no mass turnover is assumed for them. However, because the second term on the left-hand side of Eq. 15 is never null, SMCs continuously undergo remodeling, leading to a continuous update of their reference configuration.

2.3 Finite element implementation

The proposed model was implemented within the commercial FE software Abaqus (Hibbit and Sorensen 2011) through a coupled user material subroutine (UMAT) (Farzaneh et al. 2015). A 3D structural mesh made of hexahedral elements was reconstructed across the wall of the artery. The mesh was structural, which means that the edge of each element was locally aligned with the material directions of the artery: radial, circumferential and axial. For non-perfectly cylindrical geometries, the radial direction is defined as the outward normal direction to the luminal surface, the axial direction is defined as the direction parallel to the luminal centerline in the direction of the blood flow, and the circumferential direction is perpendicular to the two previously defined directions. It is assumed that each element is a mixture of elastin, collagen and SMCs with mass density varying regionally.

The deformation of the artery is computed for every time step corresponding to 1 month of real time. It is obtained by feeding equilibrium equations with the constitutive equations introduced previously and solving the resulting nonlinear equations using the Newton–Raphson method. G&R deformations tensors are obtained at each time step based on stresses assessed at the previous step. Only the initial time step is assumed to satisfy homeostatic conditions.

3 Numerical applications

Three different models were considered:

1. The first case was an thick-wall cylindrical artery responding to localized elastin loss. It was initially solved by Braeu et al. (2017) using the homogenized CMM, and the purpose was to use these previous results for validating our model.
2. The second case was a thick-wall toric artery responding to localized elastin loss. The toric model was previously used by Alford and Taber (2008) to study G&R in the aortic arch.
3. The third case was a thick-wall patient-specific artery responding to localized elastin loss.

Table 1 Material parameters employed for a single-layer thick-wall cylindrical artery and a two-layer thick-wall toric artery (Braeu et al. 2017)

Symbol	Values
$\alpha^{c_j}, j = 1, 2, \ldots, 4$	$0, \frac{\pi}{2}$ and $\pm\frac{\pi}{4}$
μ^{e}	72 (J/kg)
κ	720 (J/kg)
$k_1^{\text{c}_j}$	568 (J/kg)
$k_2^{\text{c}_j}$	11.2
k_1^{m}	7.6 (J/kg)
k_2^{m}	11.4
ϱ_0^{e}	241.5 (kg/m^3)
$\varrho_0^{\text{c}_1}$	65.1 (kg/m^3)
$\varrho_0^{\text{c}_2}$	65.1 (kg/m^3)
$\varrho_0^{\text{c}_3} = \varrho_0^{\text{c}_4}$	260.4 (kg/m^3)
ϱ_0^{m}	157.5 (kg/m^3)
λ_z^{e}	1.25
λ^{c_j}	1.062
λ^{m}	1.1
T^{e}	101 (years)
T^{c_j}	101 (days)
T^{m}	101 (days)
L_{dam}	10 (mm)
t_{dam}	40 (days)
D_{max}	0.5

α^{c_1}, α^{c_2}, α^{c_3} and α^{c_4} are axial, circumferential and two diagonal directions of collagen fiber families, respectively

Previous work with the homogenized CMM considered a single layer to model the artery. Similar single-layer models were used in the first case using material properties taken from Braeu et al. (2017) and are reported in Table 1. In other cases, in order to have a more realistic model of G&R, we considered two-layer thick-wall arteries, with different material properties for the media and the adventitia. Additional material parameters used in the two-layer thick-wall model were calibrated with data of our group (Davis et al. 2016; Mousavi et al. 2018); they are reported in Table 2.

3.1 Application to a single-layer thick-wall cylindrical artery responding to elastin loss

An idealized single-layer thick-wall cylindrical artery with $r = 10$ mm and $h = 1.41$ mm was considered. It was assumed that this geometry, which was set as the reference configuration, was related to a reference pressure of 13.3 kPa and was at homeostasis. The deposition stretch of elastin permitting to obtain mechanical equilibrium in the reference configuration was solved using the algorithm presented in Mousavi and Avril (2017). Following Braeu et al. (2017), elastin was degraded with the following rate:

Table 2 Material parameters employed for two-layer patient-specific human ATAA model adapted from Mousavi et al. (2018)

Symbol	Values
$\alpha^{c_j}, j = 1, 2, \ldots, 4$	$0, \frac{\pi}{2}$ and $\pm\frac{\pi}{4}$
μ^{e}	82 (J/kg)
κ	$100\mu^{\mathrm{e}}$ (J/kg)
$k_1^{c_j,\mathrm{c}} = k_1^{\mathrm{m,c}}$	15 (J/kg)
$k_2^{c_j,\mathrm{c}} = k_2^{\mathrm{m,c}}$	1.0
$k_1^{c_j,\mathrm{t}}$	105 (J/kg)
$k_2^{c_j,\mathrm{t}}$	0.13
$k_1^{\mathrm{m,t}}$	10 (J/kg)
$k_2^{\mathrm{m,t}}$	0.1
ϱ_0^{e}	250 (kg/m^3)
$\varrho_0^{c_j}$	460 (kg/m^3)
ϱ_0^{m}	280 (kg/m^3)
λ_z^{e}	1.3
λ^{c_j}	1.1
λ^{m}	1.1
T^{e}	101 (years)
T^{c_j}	101 (days)
T^{m}	101 (days)
t_{dam}	20, 40 and 80 (days)
$D_{\max}$	0.5

α^{c_1}, α^{c_2}, α^{c_3} and α^{c_4} are axial, circumferential and two diagonal directions of collagen fiber families, respectively

$$\dot{D}_{\mathrm{g}}^{\mathrm{e}}(\mathbf{X},t) = -\frac{\varrho^{\mathrm{e}}(\mathbf{X},t)}{T^{\mathrm{e}}} - \frac{D_{\max}}{t_{\mathrm{dam}}}\varrho^{\mathrm{e}}(\mathbf{X},0)e^{-0.5\left(\frac{X_3}{L_{\mathrm{dam}}}\right)^2 - \frac{t}{t_{\mathrm{dam}}}} \quad (17)$$

where L_{dam} and t_{dam} are the spatial and the temporal damage spread parameters, respectively, while $D_{\max}$ is maximum damage. X_3 is the material position in the axial direction of the cylinder. Due to symmetric geometry one-fourth of the cylinder was modeled using symmetric boundary conditions. The axial direction was defined such as $0 \leq X_3 \leq \frac{L}{2}$. The first term in Eq. 17 denotes a normal elastin loss by age, while the second one is related to a sudden and abnormal local damage starting at $t = 0$ with maximum value at the center of the cylinder ($X_3 = 0$) and fading at $X_3 = \frac{L}{2}$. The 3D results obtained with our model on this case are compared with the corresponding 3D results of Braeu et al. (2017) for six different growth parameters, $k_\sigma^{c_j}$.

3.2 Application to a two-layer thick-wall toric artery responding to elastin loss

We employed the model on a torus shown in Fig. 2 with $\frac{R}{r} = 4$. Its thickness and inner radius were assumed identical to the ones of the cylindrical artery defined in Sect. 3.1 ($r = 10$ mm and $h = 1.41$ mm). Due to symmetry only a quarter of the torus was modeled using symmetric boundary conditions.

Again, it was assumed that this geometry, which was set as the reference configuration, was related to a reference pressure of 13.3 kPa and was at homeostasis. The deposition stretch of elastin permitting to obtain mechanical equilibrium in the reference configuration was solved using the algorithm presented in Maes et al. (2019) and Mousavi and Avril (2017).

Then, an elastin degradation rate with temporal and spatial damage was assumed as

$$\dot{D}_{\mathrm{g}}^{\mathrm{e}}(\mathbf{X},t) = -\frac{\varrho^{\mathrm{e}}(\mathbf{X},t)}{T^{\mathrm{e}}} - \frac{D_{\max}}{t_{\mathrm{dam}}}\varrho^{\mathrm{e}}(\mathbf{X},0)e^{-0.5\left(\frac{\theta}{\theta_{\mathrm{dam}}}\right)^2 - \frac{t}{t_{\mathrm{dam}}}} \quad (18)$$

where θ_{dam} is the spatial damage spread parameters. $0 \leq \theta \leq 90$ is the material position varying as shown in Fig. 2, indicating maximal and minimal elastin loss at $\theta = 0°$ and $\theta = 90°$, respectively.

Material parameters reported in Table 1 were employed considering that the media comprised 97% of total elastin, 100% of total SMCs and 15% of total axial and diagonal collagen fibers, while the adventitia comprised 3% of total elastin, 85% of total axial and diagonal collagen and 100% of total circumferential collagen (Bellini et al. 2014).

3.3 Application to a two-layer thick-wall patient-specific human ATAA responding to elastin loss

To demonstrate the applicability of the model to predict patient-specific wall G&R, the model was employed onto the geometry of a real human ATAA. An ATAA specimen and the preoperative CT scan of the patient were obtained after

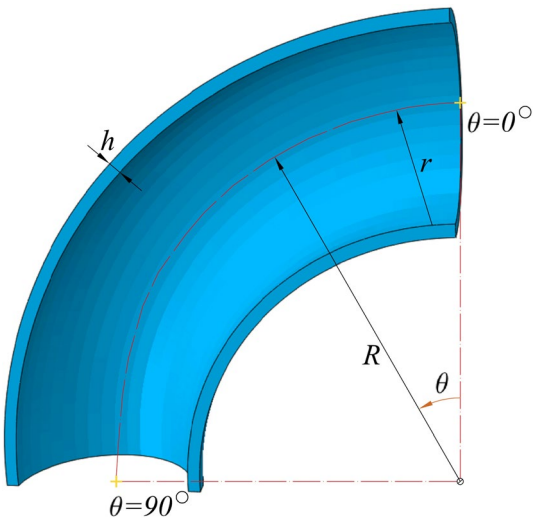

Fig. 2 Schematic display of an arch on which the presented G&R model is applied

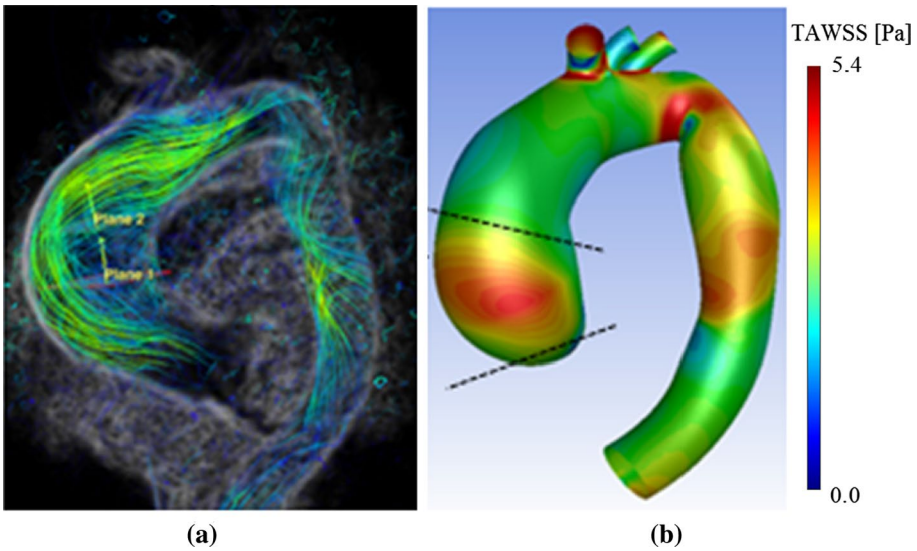

Fig. 3 A jet flow impingement against the aortic wall was observed around the bulge region in the 4D flow MRI (**a**) causing the maximum TAWSS in that region (**b**) based on CFD analysis by Condemi et al. (2017)

informed consent from a donor undergoing elective surgery for ATAA repair at CHU-SE (Saint-Etienne, France). The lumen of the aneurysm was clearly visible in the DICOM file, but detection of the aneurysm surface was not possible automatically. A non-automatic segmentation of the CT image slices was performed using MIMICS (v. 10.01, Materialise NV) to reconstruct the ATAA geometry. The reconstructed geometry was meshed with 7700 hexahedral elements. A wall thickness of 2.38 mm was defined evenly in the reference configuration, yielding an average thickness of 2.67 mm at zero pressure, which corresponded to the measured thickness on the supplied sample (Farzaneh et al. 2018). Material parameters (reported in Table 2) such as deposition stretch of collagen and exponents were taken from the literature (Bellini et al. 2014; Cardamone et al. 2009), and others were calibrated with data of our group (Davis et al. 2016). Note that 97% of total elastin, 100% of total SMC and 15% of total axial and diagonal collagen fibers were assigned to the media. Conversely, 3% of total elastin, 85% of total axial and diagonal collagen and 100% of total circumferential collagen were assigned to the adventitia (Bellini et al. 2014; Mousavi and Avril 2017; Mousavi et al. 2018). The geometry obtained from the CT scan was assigned as the reference configuration. It was subjected to a luminal pressure of 80 mmHg (diastole). An axial deposition stretch of 1.3 was defined for the elastin and the deposition stretches of collagen and SMC components were set to 1.1. The spatially varying circumferential deposition stretch of elastin was determined to ensure equilibrium with the luminal pressure using our iterative algorithm (Mousavi and Avril 2017). Both ends of the ATAA model were fixed in axial and circumferential directions, allowing only radial displacements.

4D flow magnetic resonance imaging (MRI) with full volumetric coverage of ATAAs can reveal complex aortic 3D blood flow patterns, such as flow jets, vortices and helical flow (Condemi et al. 2017; Hope et al. 2007). For the same patient, 4D flow MRI datasets were also acquired, revealing a jet flow impingement against the aortic wall around the bulge region (downstream the area of maximum dilatation) as shown in Fig. 3a. Guzzardi et al. (2015) found that regions with largest WSS underwent greater elastin degradation associated with vessel wall remodeling in comparison with the adjacent regions with normal WSS. Consequently, based on these findings we considered a localized elastin degradation and simulated its effects on ATAA G&R. The local elastin degradation rate was written as

$$\dot{D}_{\mathrm{g}}^{\mathrm{e}}(\mathbf{X},t) = -\frac{\varrho^{\mathrm{e}}(\mathbf{X},t)}{T^{\mathrm{e}}} - \frac{D_{\max}}{t_{\mathrm{dam}}}\varrho^{\mathrm{e}}(\mathbf{X},0)e^{-\frac{t}{t_{\mathrm{dam}}}} \tag{19}$$

Three different values of t_{dam} (as listed in Table 2) were studied.

4 Results

4.1 Response of a single-layer thick-wall cylindrical artery to localized elastin loss

The dilatation at the middle of the cylindrical artery (where maximum elastin loss occurs) is shown in Fig. 4 over 15 years for different growth parameters. There are a good agreement between these results obtained with our 3D FEM and the numerical model from Braeu et al. (2017). The cylindrical artery responds to elastin degradation with large and unstable dilatations for small gain parameters, while it only slightly dilates in the case of relatively large gain parameters, recovering its stability after a transient period. Distribution of maximum principal stresses and distributions of normalized collagen mass density for the largest and smallest gain

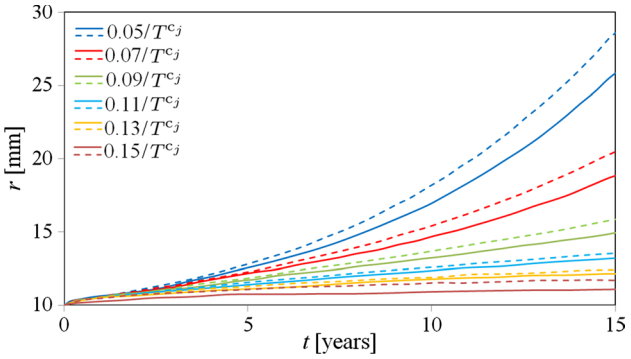

Fig. 4 Dilatation of a single-layer thick-wall cylindrical artery responding to elastin loss for different growth parameters. The dilatation is plotted for the point where maximum elastin loss occurs). Numerical results obtained by Braeu et al. (2017) (dash lines) were compared to the results obtained our 3D Abaqus model (solid lines)

parameters are shown in Fig. 5. Elastin loss naturally leads to higher stresses in the other components of the arterial wall and subsequently higher deposition of new collagen fibers.

4.2 Response of a two-layer thick-wall toric artery to localized elastin loss

The effect of elastin loss during 15 years in a two-layer toric artery was considered for $k_\sigma^{c_j} = \frac{0.05}{T^{c_j}}$ and $k_\sigma^{c_j} = \frac{0.15}{T^{c_j}}$. The changes in the thickness and diameter due to degradation of the elastin are shown in Fig. 6a, b, respectively. The dilatation and thickness were never stable for small growth parameters ($k_\sigma^{c_j} = \frac{0.05}{T^{c_j}}$). Conversely, for relatively large growth parameters ($k_\sigma^{c_j} = \frac{0.15}{T^{c_j}}$), the thickness and diameter became stable after about 5 years of transient growth period. The wall was basically thickened on the outer curvature side, mainly in the media. Therefore, the response of a toric artery

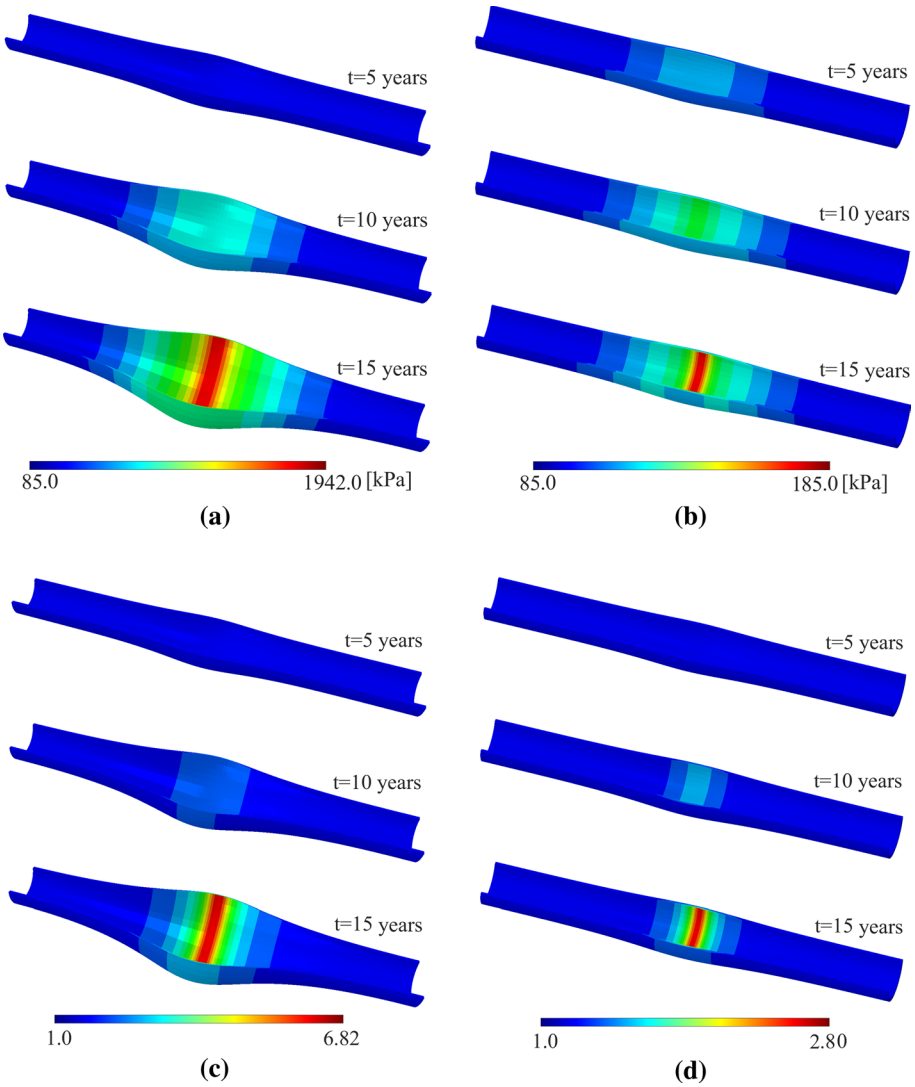

Fig. 5 Distribution of the maximum principal stress (**a**, **b**) and normalized collagen mass density (**c**, **d**) in a single-layer thick-wall cylindrical artery responding to an elastin loss during 15 years, $k_\sigma^{c_j} = \frac{0.05}{T^{c_j}}$ (first column) and $k_\sigma^{c_j} = \frac{0.15}{T^{c_j}}$ (second column)

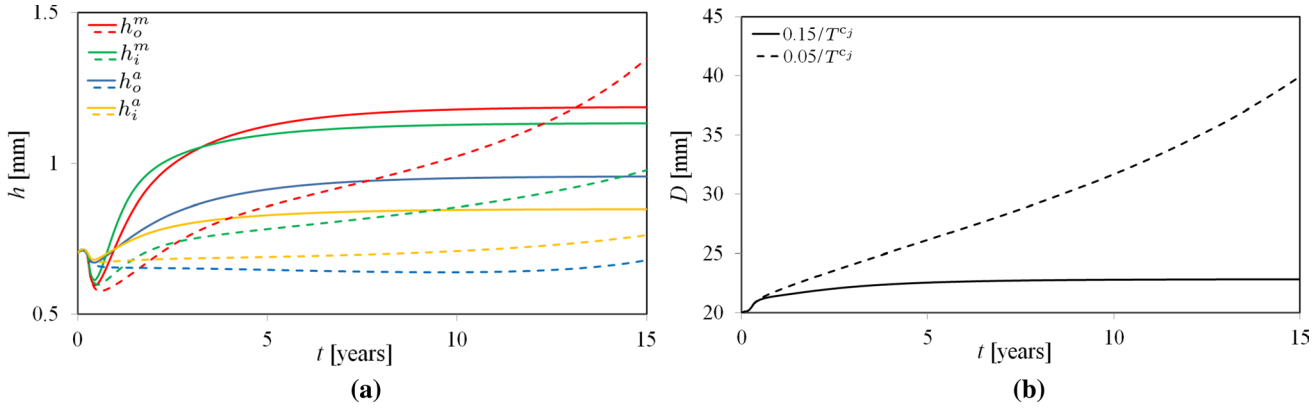

Fig. 6 Change in thickness (**a**) and diameter (**b**) of a two-layer thick-wall toric artery responding to elastin loss during 15 years for $k_\sigma^{c_j} = \frac{0.05}{T^{c_j}}$ (dash lines) and $k_\sigma^{c_j} = \frac{0.15}{T^{c_j}}$ (solid lines). Superscripts "m" and "a" stand for media and adventitia, respectively, while subscripts "i" and "o" denote the inner and outer curvatures of the arch, respectively

to elastin loss is unstable for small growth parameters, while it recovers its stability, after some enlargement, for relatively large growth parameters. In addition, color maps of the maximum principal stress and the collagen mass density for large and small growth parameters (Fig. 7) show that elastin loss continuously causes higher stresses and collagen deposition in the media. However, the balance between arterial dilatation and collagen deposition leads to higher collagen production for small gain parameters. This in turn ends with higher stresses in the arch with small gain parameters.

4.3 Response of a two-layer patient-specific human ATAA to localized elastin loss

The G&R response of a patient-specific ATAA to localized elastin degradation is shown in Fig. 8a, c and e. Due to change in shape, the stress distribution is in continuous adaptation. For all cases, elastin loss induces a transfer of stress to the adventitia in the damaged region. Moreover, an increase in t_{dam} results in an increase in maximum principal stresses in the arterial wall. It is induced by the related increase in elastin degradation rate. In Fig. 8b, d and f, the distribution of collagen mass density for different t_{dam} shows that most of the collagen is deposited in the media where elastin has been lost (recall that ~97% of the elastin is in media), causing finally a thickening of the arterial wall (Fig. 9). It is noteworthy that the increase in t_{dam} accelerates collagen deposition and consequently wall thickening. Moreover, we studied the sensitivity of ATA dilatation to the collagen growth parameter, $k_\sigma^{c_j}$. As shown in Fig. 10, larger growth parameters stabilize ATA dilatation induced by elastin loss. However, for relatively small growth parameters, $k_\sigma^{c_j} = \frac{0.1}{T^{c_j}}$, as shown in Figs. 10a, b and 11a, the ATA undergoes an excessive dilatation. (The maximum ATA diameter increases continuously from ~ 42 to ~ 64 mm after ~180 months.) As the newly deposited collagen has to compensate for the elastin loss to maintain the homeostatic state, this induces the adaptation response. Conversely, increasing the growth parameter leads to a stable growth of ATA after 31 months. (The maximum diameter of ATA after elastin loss stops increasing after ~31 months, enlarging from ~ 42 to ~ 47 mm.) For all cases, whatever the growth parameter, remodeling induced by collagen deposition always causes ATA wall thickening, mainly in the media (see Fig. 11).

5 Discussion

A robust computational model based on the homogenized CMT was presented and its potential was shown to predict ATAA evolution for a patient-specific aortic geometry, showing that the typical shape of an ATAA can be obtained simply with a proteolysis of elastin localized in regions of deranged hemodymanics. The most interesting result is that although elastin degradation occurs locally in the ATAA at the location of WSS peak, the whole ATAA globally undergoes G&R due to redistribution of stresses distribution, leading to ATAA dilatation.

A general advantage of the model presented here is that it was developed to account for in situ prestrain (and therefore prestress). It permits to run FE analysis of G&R in soft biological tissues without requiring a zero-pressure configuration. This appears to be especially beneficial when a patient-specific geometry is reconstructed using CT scans or MRI data acquired in a pressurized configuration. Using this methodology, the prestress is calculated based on the prestrain, defined in terms of fiber prestretches (deposition stretches), assuming a hyperelastic elastic material behavior. Therefore, a drawback of this methodology is that we may encounter some instability in the resolution if we enforce

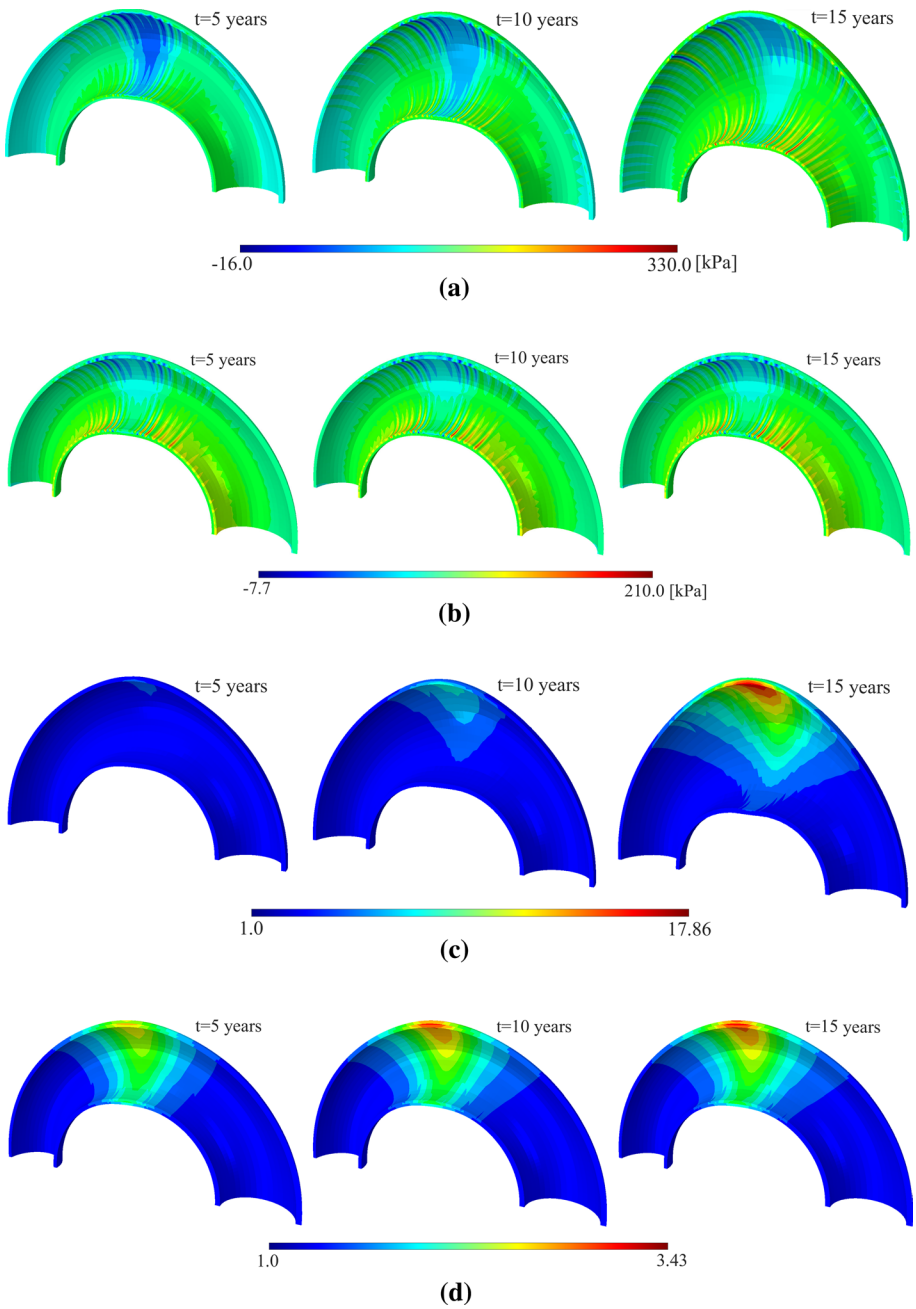

Fig. 7 Distribution of maximum principal stress (**a**, **b**) and normalized collagen mass density (**c**, **d**) in a two-layer thick-wall toric artery responding to elastin loss during 15 years, $k_\sigma^{c_j} = \frac{0.05}{T^{c_j}}$ (**a**, **c**) and $k_\sigma^{c_j} = \frac{0.15}{T^{c_j}}$ (**b**, **d**)

a particular deposition stretch for each constituent. Large distortions of elements may also occur with small variations of deposition stretches and lead to the divergence of the resolution. This indicates that an arbitrary deposition stretch cannot be always imposed on an arbitrary reference configuration.

For all geometries given herein for large gain parameters, k_σ, the blood vessel recovered a new stable state after a transient period of dilation and enlargement. In contrast, for small gain parameters it underwent unbounded dilation, experiencing mechanobiological instability. Dilatation due to weakening of the arterial wall by elastin loss is physically consistent with previous findings (Braeu et al. 2017; Cyron et al. 2016). However, one can find 3D FE implementation of G&R in which the arterial radius decreases after elastin degradation (Eriksson et al. 2014; Grytsan et al. 2015; Valentín et al. 2013). This can be explained by the implementation of volumetric growth. Eriksson et al. (2014), Grytsan et al. (2015) and Valentín et al. (2013) defined implicitly the growth directions using the volumetric deviatoric contributions of the deformation gradient and imposing incompressibility constraints. Only isotropic growth can be modeled with their approach, elastin degradation consequently causing a decrease in total tissue volume. Therefore, in

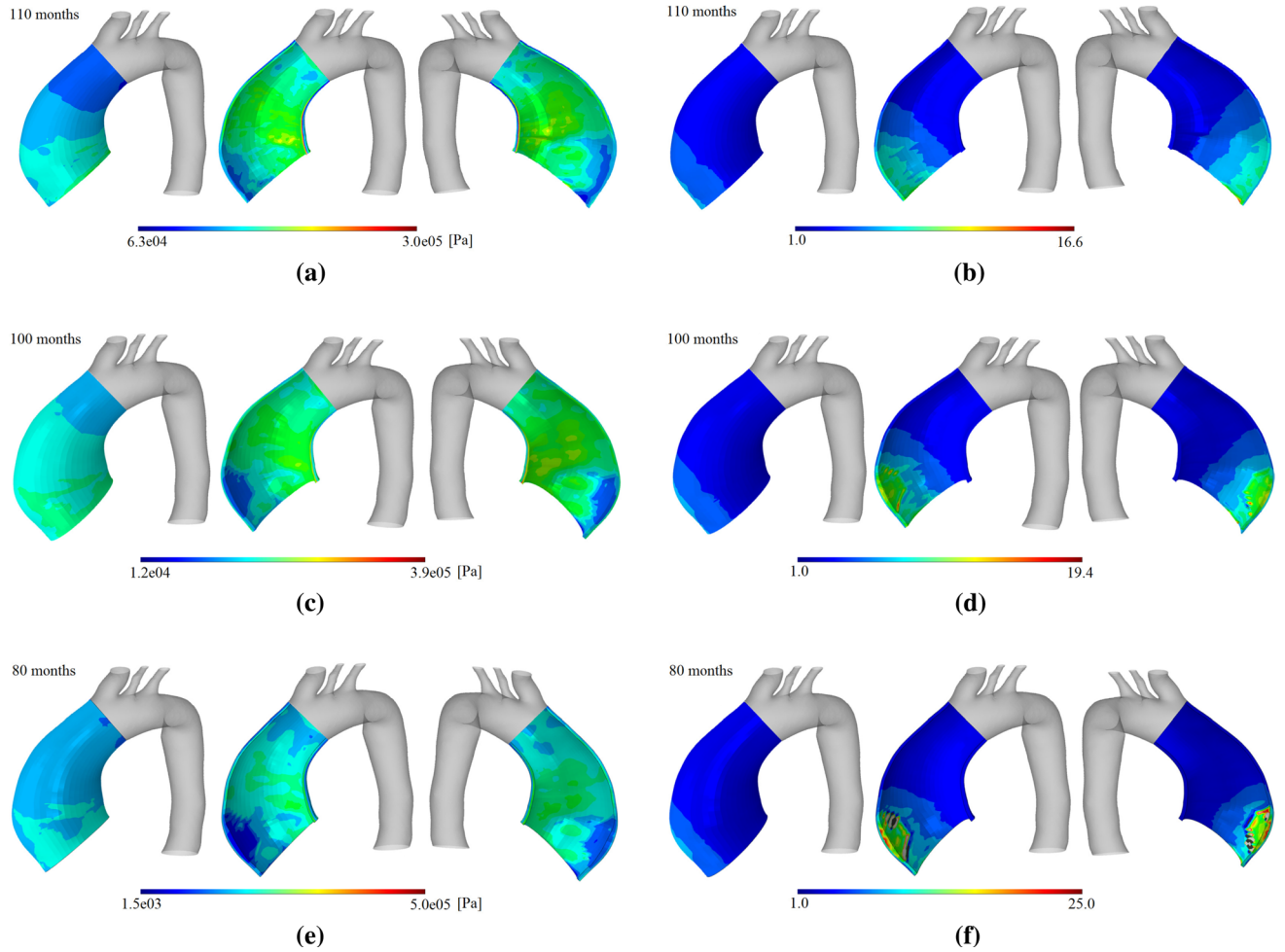

Fig. 8 Distribution of the maximum principal stress (first column) and normalized collagen mass density (second column) in a two-layer patient-specific human ATAA responding to localized elastin loss, $t_{\text{dam}} = 20$ (**a**, **b**), $t_{\text{dam}} = 40$ (**c**, **d**) and $t_{\text{dam}} = 80$ (**e**, **f**) days. In all cases, it is assumed that $k_{\sigma}^{c_j} = \frac{0.05}{T^{c_j}}$

their model the arterial wall shrinks in all spatial directions, including the circumferential direction. Eriksson (2014) attempted to overcome this problem by introducing the concept of constant and adaptive individual density growth in which an elastin loss does not cause a contraction of the arterial wall due to loss of mass. Nevertheless, it is still controversial whether elastin loss would locally lead to arterial shrinking in the thickness direction or whether it would really induce a change in the mass density of the tissue.

Basically, two major approaches were so far proposed for numerical modeling of soft tissue G&R. Rodriguez and Hoger (1994) introduced a kinematic growth theory by multiplicative decomposition of the deformation gradient into an elastic and an inelastic growth contributions. The elastic part ensured geometric compatibility and mechanical equilibrium, while the inelastic growth part contained the local changes in mass and volume. Although their model was computationally efficient and conceptually simple, it was intrinsically unable to compute the separate G&R of structurally different constituents. This limitation was fixed by CMT-based model introduced by Humphrey and Rajagopal (2002) in which the in vivo situation can be realistically mimicked using the concept of deposition stretches. The computational cost of the classical CMT-based models is higher than that of simple kinematic growth theory. Homogenized CMT-based models introduced by Cyron et al. (2016) combines the advantages of both classical CMT-based models and simple kinematic growth models to overcome the drawback of each model. The results obtained by homogenized CMT-based models are similar to the classical ones but with low computational cost. Focusing on the example of simple membrane-like (Cyron et al. 2016) and thick-wall (Braeu et al. 2017) cylindrical vessels, they showed that homogenized CMT-based models are able to reproduce realistically both pathological growth responding to an elastin loss (as observed in aneurysms) and adaptive growth in

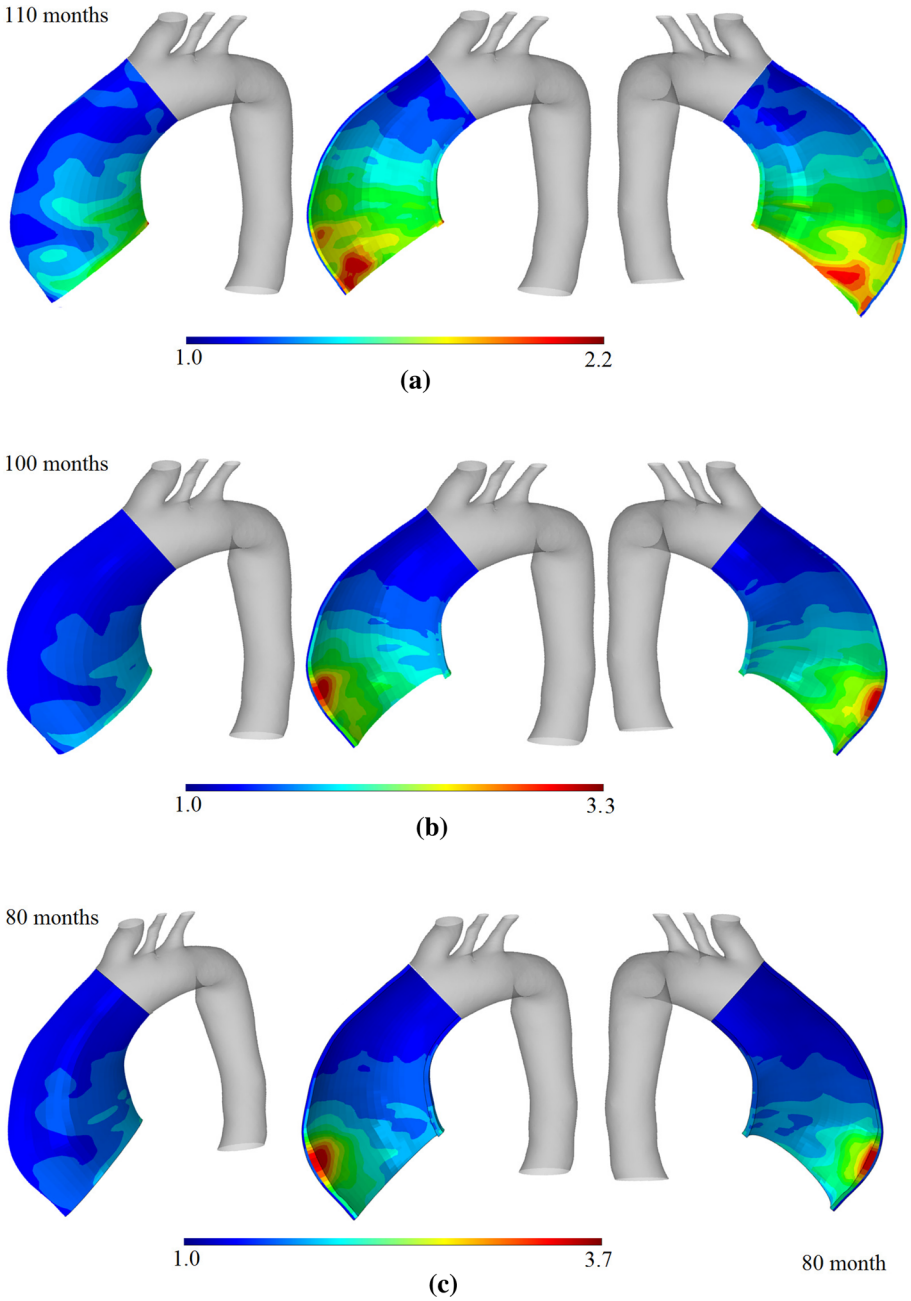

Fig. 9 Distribution of the normalized thickness in a two-layer patient-specific human ATAA responding to localized elastin loss for **a** $t_{\text{dam}} = 20$, **b** $t_{\text{dam}} = 40$ and **c** $t_{\text{dam}} = 80$ days. In all cases, it is assumed that $k_{\sigma}^{c_j} = \frac{0.05}{T^{c_j}}$

healthy vessels due to hypertension. The prominent privilege of CMT-based models is the inherent incorporation of anisotropic volumetric growth in the thickness direction of arterial wall (proved by experimental observations of Matsumoto and Hayashi (1996)). Moreover, recently Lin et al. (2017) have combined homogenization and CMT to capture G&R of the abdominal aorta and to consider dilatation of abdominal aortic aneurysms under loading. They focused on a transversely isotropic mixture subjected to uniform extension in the direction of collagen fibers assuming that they are embedded in an isotropic elastin matrix, ignoring the role of SMCs. Considering a very special case of isotropic growth, their model can successfully predict the continuous enlargement of an abdominal aortic aneurysm by combined effects of elastin degradation, loss of extant collagen and production of new collagen, as well as fiber remodeling.

As anisotropic growth may stabilize the arterial wall under perturbations more efficiently than the isotropic growth (Braeu et al. 2017), the ability of the homogenized CMT-based model implemented herein can be considered an ideal tool to realistically study the patient-specific geometries undergoing G&R in response to an unexpected degradation of elastin. Following Braeu et al. (2017), Bellini et al. (2014), Cardamone et al. (2009), Watton and Hill (2009) and

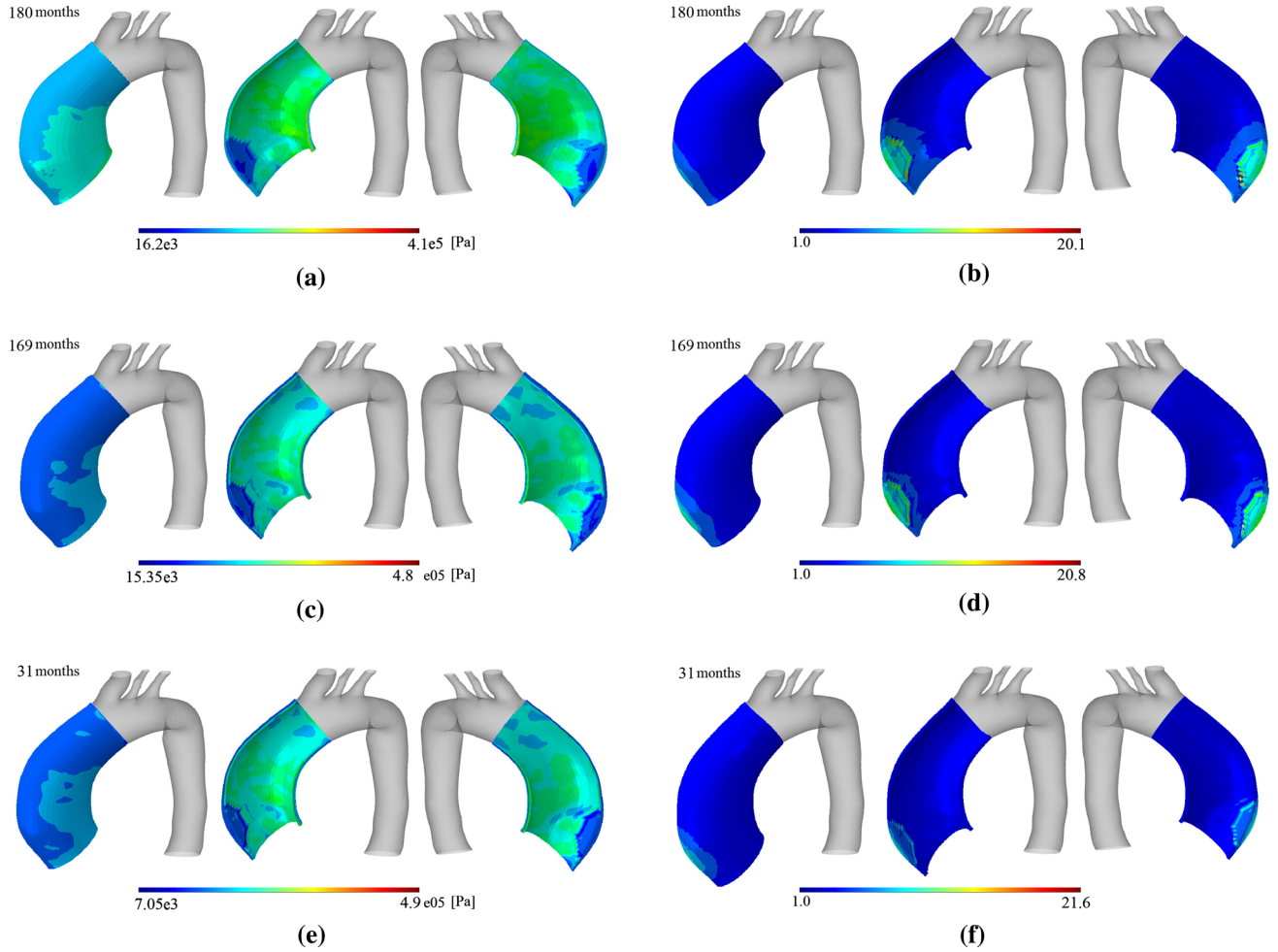

Fig. 10 Distribution of the maximum principal stress (first column) and normalized collagen mass density (second column) in a two-layer patient-specific human ATAA responding to localized elastin loss, $k_\sigma^{c_j} = \frac{0.1}{T^{c_j}}$ (**a**, **b**), $k_\sigma^{c_j} = \frac{0.2}{T^{c_j}}$ (**c**, **d**) and $k_\sigma^{c_j} = \frac{0.3}{T^{c_j}}$ (**e**, **f**) days. In all cases, it is assumed that $t_{\text{dam}} = 40$

Watton et al. (2004), it was assumed that patient-specific G&R resulted from specific temporal and spatial distributions of elastin degradation. We considered multiple temporal damage parameters for elastin degradation leading to different aneurysm growth rate. Although the global shape of the aneurysm resembles, the thickening and collagen production rates are different for different cases. Different temporal damage constants showed significant effects on the expansion rate where the higher t_{dam} delivers the higher G&R rate. Although we simply employed temporal damage parameter for elastin degradation, elastin degradation during ATAA growth involves multiple biological and mechanical parameters including abnormal distribution of wall shear stress (Guzzardi et al. 2015) and circumferential stress (Humphrey and Rajagopal 2002). The formation of intraluminal thrombus is specific to AAA (Vorp and Geest 2005; Vorp et al. 2001). It may stimulate proteolytic effects, but this was not considered here as thrombus are very rare in ATAAs.

In the patient-specific study, it also appears that collagen deposition tends to compensate the elastin loss. It is worth noting that as aneurysm grows, principal stress may not increase necessarily in a damaged location. This is observed in AAA growth as well (Zeinali-Davarani et al. 2011). Moreover, although elastin was degraded locally, dilatation of the ATA was spread across a larger area due to stress redistribution.

The in vivo images were obtained when the artery was under pressure so that the stress-free or zero-pressure configuration was not basically available. Hence, for hyperelastic models such as Holzapfel-type models (Holzapfel et al. 2000), approaches such as inverse elastostatic methods (Zhou et al. 2010) or Lagrangian–Eulerian formulations (Gee et al. 2010) are required to estimate the stress-free state of in vivo geometries obtained from medical images. One of the advantages of current CMT-based model is that G&R analysis of a patient-specific model can be directly

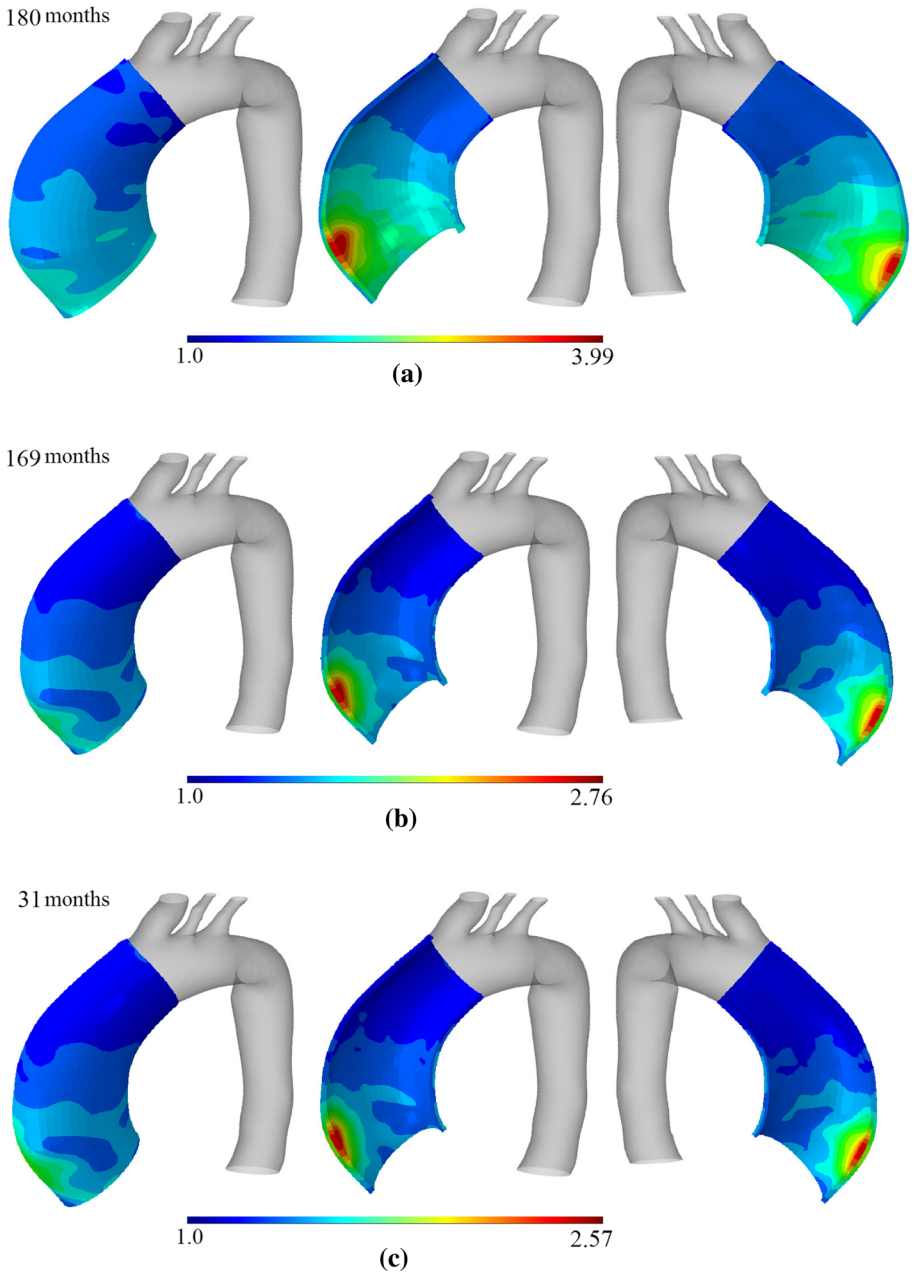

Fig. 11 Distribution of the normalized thickness in a two-layer patient-specific human ATAA responding to localized elastin loss for **a** $k_\sigma^{c_j} = \frac{0.1}{T^{c_j}}$, **b** $k_\sigma^{c_j} = \frac{0.2}{T^{c_j}}$ and **c** $k_\sigma^{c_j} = \frac{0.3}{T^{c_j}}$ days. In all cases, it is assumed that $t_{\text{dam}} = 40$

performed on the in vivo geometry reconstructed from medical images obtained under pressure, without needing to compute the stress-free geometry.

Salient features of the response of arterial walls to altered hemodynamics (Baek et al. 2006, 2007; Cardamone et al. 2010; Valentín et al. 2009) were captured by 2D and 3D CMT-based models (Cardamone and Humphrey 2012; Humphrey and Rajagopal 2002; Karšaj et al. 2010). Despite the major interest of this prior work on CMT-based models, two novelties can be highlighted in our work: application of CMT-based models to patient-specific geometries and integration of layer-specific properties (media and adventitia). Future work will focus on fully coupling the present model with CFD analyses (Condemi et al. 2017) to study the effects on aortic G&R of different hemodynamic metrics, such as helicity, wall shear stress (WSS), time-averaged WSS (TAWSS), oscillatory shear index (OSI) or relative residence time (RRT). Such fluid–solid growth simulations have already been developed by different authors for cerebral (Watton et al. 2009) or abdominal (Di Achille et al. 2017; Grytsan et al. 2015; Marsden and Feinstein 2015; Sheidaei et al. 2011) aneurysms, and we will extend them to ATAA to provide additional insight into the evolution of these aneurysms.

This altogether indicates that the present model has the potential for clinical applications to predict G&R of patient-specific geometries if a realistic rate of elastin loss and collagen growth parameter is available.

There are still several limitations and technical challenges associated with current model:

- The active role of SMCs is not considered in the present model, despite its major role in mechanosensing (Humphrey et al. 2015).
- Theory of G&R is based on a key assumption, the existence of mechanical homeostasis (Kassab 2008; Humphrey 2008b). It is difficult to have the assumption of a homeostatic state satisfied at every point of the arterial wall. For an idealized model, such as ideal thick-wall cylinders, the in vivo material properties are typically assumed to be uniform across the domain. When a patient-specific geometry is used for a clinical study, it will be essential to prescribe the distribution of material and structural parameters such as thickness and fiber orientations consistent with in vivo data. Therefore, the arterial wall with a uniform thickness can be considered as additional limitations of the current work.
- Another difficulty associated with patient-specific models is estimating the constitutive parameters of the model for different patients. Here, these parameters were estimated by curve fitting from the ex vivo bulge inflation data of an ATAA segment excised after the surgical intervention of the same patient. However, in clinical applications, it will be needed to identifying noninvasively the in vivo material properties of ATAAs (Farzaneh et al. 2018, 2019).

6 Conclusion

In summary, in this manuscript, a robust computational model based on the homogenized CMT was presented and its potential was shown for patient-specific predictions of growth and remodeling of aneurysmal human aortas in response to localized elastin loss. As future application, the predictions of this G&R framework will be validated on datasets of patient-specific ATAA geometries followed up over a significant number of years.

Acknowledgements The authors are grateful to the European Research Council for Grant ERC-2014-CoG BIOLOCHANICS. The authors would also like to thank Nele Famaey (KU Leuven, Belgium), Christian J. Cyron (TU Hamburg, Germany) and Fabian A. Braeu (TU München, Germany) for inspiring discussions related to this work.

Compliance with ethical standards

Conflict of interest The authors declare that they have no conflict of interest.

References

Alford PW, Taber LA (2008) Computational study of growth and remodelling in the aortic arch. Comput Methods Biomech Biomed Eng 11(5):525–38

Baek S, Rajagopal KR, Humphrey JD (2006) A theoretical model of enlarging intracranial fusiform aneurysms. J Biomech Eng 128(1):142–9

Baek S, Valentín A, Humphrey JD (2007) Biochemomechanics of cerebral vasospasm and its resolution: II. Constitutive relations and model simulations. Ann Biomed Eng 35:1498-509

Bellini C, Ferruzzi J, Roccabianca S, Di Martino ES, Humphrey JD (2014) A microstructurally motivated model of arterial wall mechanics with mechanobiological implications. Ann Biomed Eng 42(3):488–502

Bersi MR, Bellini C, Di Achille P, Humphrey JD, Genovese K, Avril S (2016) Novel methodology for characterizing regional variations in the material properties of murine aortas. J Biomech Eng 138(7):11. https://doi.org/10.1115/1.4033674

Braeu FA, Seitz A, Aydin RC, Cyron CJ (2017) Homogenized constrained mixture models for anisotropic volumetric growth and remodeling. Biomech Model Mechanobiol 16(3):889–906

Cardamone L, Humphrey JD (2012) Arterial growth and remodelling is driven by hemodynamics. In: Ambrosi D, Quarteroni A, Rozza G (eds) Modeling of physiological flows, MS&A—modeling, simulation and applications. Springer, Milan

Cardamone L, Valentin A, Eberth JF, Humphrey JD (2009) Origin of axial prestretch and residual stress in arteries. Biomech Model Mechanobiol 8:431–46

Cardamone L, Valentín A, Eberth JF, Humphrey JD (2010) Modelling carotid artery adaptations to dynamic alterations in pressure and flow over the cardiac cycle. Math Med Biol 27(4):343–71

Comellas E, Gasser TC, Bellomo FJ, Oller S (2016) A homeostatic-driven turnover remodelling constitutive model for healing in soft tissues. J R Soc Interface 13(116):12. https://doi.org/10.1098/rsif.2015.1081

Condemi F, Campisi S, Viallon M, Troalen T, Xuexin G, Barker AJ, Markl M, Croisille P, Trabelsi O, Cavinato C, Duprey A, Avril S (2017) Fluid- and biomechanical analysis of ascending thoracic aorta aneurysm with concomitant aortic insufficiency. Ann Biomed Eng 45(12):2921–32

Cyron CJ, Humphrey JD (2016) Growth and remodeling of load-bearing biological soft tissues. Meccanica 52(3):645–64

Cyron CJ, Wilson JS, Humphrey JD (2014) Mechanobiological stability: a new paradigm to understand the enlargement of aneurysms? J R Soc Interface 11(100):20140680

Cyron CJ, Aydin RC, Humphrey JD (2016) A homogenized constrained mixture (and mechanical analog) model for growth and remodeling of soft tissue. Biomech Model Mechanobiol 15(6):1389–1403

Davis FM, Luo Y, Avril S, Duprey A, Lu J (2016) Local mechanical properties of human ascending thoracic aneurysms. J Mech Behav Biomed Mater 61:235–49

Di Achille P, Tellides G, Humphrey JD (2017) Hemodynamics-driven deposition of intraluminal thrombus in abdominal aortic aneurysms. Int J Numer Method Biomed Eng 33(5):e2828

Eriksson TSE (2014) Modelling volumetric growth in a thick-walled fibre reinforced artery. J Mech Phys Solids 73:134–150
Eriksson TSE, Watton PN, Luo XY, Ventikose Y (2014) Modelling volumetric growth in a thick-walled fibre reinforced artery. J Mech Phys Solids 73:134–50
Famaey N, Vastmans J, Fehervary H, Maes L, Vanderveken E, Rega F, Mousavi SJ, Avril S (2018) Numerical simulation of arterial remodeling in pulmonary autografts. Z Angew Math Mech 98:1–19
Farzaneh S, Paseta O, Gómez-Benito MJ (2015) Multi-scale finite element model of growth plate damage during the development of slipped capital femoral epiphysis. Biomech Model Mechanobiol 14(2):371–85
Farzaneh S, Trabelsi O, Avril S (2018) Inverse identification of local stiffness across ascending thoracic aortic aneurysms. Biomech Model Mechanobiol. https://doi.org/10.1007/s10237-018-1073-0
Farzaneh S, Trabelsi O, Chavent B, Avril S (2019) Identifying local arterial stiffness to assess the risk of rupture of ascending thoracic aortic aneurysms. Ann Biomed Eng 47(4):1038–50
Figueroa CA, Baek S, Taylor CA, Humphrey JD (2009) A computational framework for fluid–solid-growth modeling in cardiovascular simulations. Comput Methods Appl Mech Eng 198(45–46):3583–602
Gasser Ch, Grytsan A (2017) Biomechanical modeling the adaptation of soft biological tissue. Curr Opin Biomed Eng 1:71–77
Gee MW, Forster C, Wall WA (2010) A computational strategy for prestressing patient-specific biomechanical problems under finite deformation. Int J Numer Meth Biomed Eng 26:52–72
Grossman W (1980) Cardiac hypertrophy: useful adaptation or pathologic process? Am J Med 69(4):576–84
Grytsan A, Watton PN, Holzapfel GA (2015) A thick-walled fluid–solid growth model of abdominal aortic aneurysm evolution: application to a patient-specific geometry. J Biomech Eng 137(3):031008
Guzzardi DG, Barker AJ, van Ooij P, Malaisrie SC, Puthumana JJ, Belke DD, Mewhort HE, Svystonyuk DA, Kang S, Verma S, Collins J, Carr J, Bonow RO, Markl M, Thomas JD, McCarthy PM, Fedak PW (2015) Valve-related hemodynamics mediate human bicuspid aortopathy: insights from wall shear stress mapping. J Am Coll Cardiol 66(8):892–900
Hibbit K, Sorensen (2011) Abaqus-theory manual, 6.11-3 edition
Holzapfel AG, Gasser CT, Ogden RW (2000) A new constitutive framework for arterial wall mechanics and a comparative study of material models. J Elast 61:1–48
Hope TA, Markl M, Wigström L, Alley MT, Miller DC, Herfkens RJ (2007) Comparison of flow patterns in ascending aortic aneurysms and volunteers using four-dimensional magnetic resonance velocity mapping. J Magn Reson Imaging 26(6):1471–9
Hosseini HS, Taber LA (2018) How mechanical forces shape the developing eye. Progr Biophys Mol Biol 137:1–12
Hosseini HS, Garcia KE, Taber LA (2017) A new hypothesis for foregut and heart tube formation based on differential growth and actomyosin contraction. Development 144(13):2381–2391
Humphrey JD (1995) Mechanics of arterial wall: review and directions. Crit Rev Biomed Eng 23(1–2):1–162
Humphrey JD (2008a) Mechanisms of arterial remodeling in hypertension: coupled roles of wall shear and intramural stress. Hypertension 52(2):195–200
Humphrey JD (2008b) Vascular adaptation and mechanical homeostatsis at tissue, cellular, and sub-cellular levels. Cell Biochem Biophys 50:53–78
Humphrey JD, Holzapfel GA (2012) Mechanics, mechanobiology, and modeling of human abdominal aorta and aneurysms. J Biomech 45(5):805–84
Humphrey JD, Rajagopal KR (2002) A constrained mixture model for growth and remodeling of soft tissues. Math Models Methods Appl Sci 12(03):407–30
Humphrey JD, Schwartz MA, Tellides G, Milewicz DM (2015) Role of mechanotransduction in vascular biology: focus on thoracic aortic aneurysms and dissections. Circ Res 116(8):1448–1461
Karšaj I, Sorić J, Humphrey JD (2010) A 3-D framework for arterial growth and remodeling in response to altered hemodynamics. Int J Eng Sci 48(11):1357–1372
Kassab GS (2008) Mechanical homeostasis of cardiovascular tissue. In: Artmann GM, Chien S (eds) Bioengineering in cell and tissue research. Springer, Berlin, pp 371–391
Latorre M, Humphrey JD (2018a) Critical roles of time-scales in soft tissue growth and remodeling. APL Bioeng 2:026108
Latorre M, Humphrey JD (2018b) Mechanobiological stability of biological soft tissues. J Mech Phys Solids 125:298–325
Lin WJ, Iafrati MD, Peattie RA, Dorfmann L (2017) Growth and remodeling with application to abdominal aortic aneurysms. J Eng Math 109(1):113–137
Maes L, Fehervary H, Vastmans J, Mousavi SJ, Avril S, Famaey N (2019) Constrained mixture modeling affects material parameter identification from planar biaxial tests. J Mech Behav Biomed Mater 95:124–35
Marsden AL, Feinstein JA (2015) Computational modeling and engineering in pediatric and congenital heart disease. Curr Opin Pediatr 27(5):587
Matsumoto T, Hayashi K (1996) Response of arterial wall to hypertension and residual stress. In: Hayashi K, Kamiya A, Ono K (eds) Biomechanics. Springer, Tokyo, pp 93–119
Mousavi SJ, Avril S (2017) Patient-specific stress analyses in the ascending thoracic aorta using a finite-element implementation of the constrained mixture theory. Biomech Model Mechanobiol. https://doi.org/10.1007/s10237-017-0918-2
Mousavi SJ, Farzaneh S, Avril S (2018) Computational predictions of damage propagation preceding dissection of ascending thoracic aortic aneurysms. Int J Numer Method Biomed Eng 34(4):e2944
Riveros F, Chandra S, Finol EA, Gasser TC, Rodriguez JF (2013) A pull-back algorithm to determine the unloaded vascular geometry in anisotropic hyperelastic aaa passive mechanics. Ann Biomed Eng 41(4):694–708
Rodriguez EK, Hoger A (1994) Stress-dependent finite growth in soft elastic tissues. J Biomech 27(4):455–67
Rodriguez JF, Ruiz C, Doblaré M, Holzapfel G (2008) Mechanical stresses in abdominal aortic aneurysms: influence of diameter, asymmetry, and material anisotropy. ASME J Biomech 130(2):021023
Sheidaei A, Hunley SC, Zeinali-Davarani S, Raguin LG, Baek S (2011) Simulation of abdominal aortic aneurysm growth with updating hemodynamic loads using a realistic geometry. Med Eng Phys 33(1):80–88
Valentín A, Holzapfel GA (2012) Constrained mixture models as tools for testing competing hypotheses in arterial biomechanics: a brief survey. Mech Res Commun 42:126–33
Valentín A, Humphrey JD (2009a) Evaluation of fundamental hypotheses underlying constrained mixture models of arterial growth and remodelling. Philos Trans A Math Phys Eng Sci 367:3585–606
Valentín A, Humphrey JD (2009b) Parameter sensitivity study of a constrained mixture model of arterial growth and remodeling. J Biomech Eng 131:101006
Valentín A, Cardamone L, Baek S, Humphrey JD (2009) Complementary vasoactivity and matrix remodelling in arterial adaptations to altered flow and pressure. J R Soc Interface 6(32):293–306
Valentín A, Humphrey JD, Holzapfel GA (2011) A multi-layered computational model of coupled elastin degradation, vasoactive dysfunction, and collagenous stiffening in aortic aging. Ann Biomed Eng 39(7):2027–45
Valentín A, Humphrey JD, Holzapfel G (2013) A finite element-based constrained mixture implementation for arterial growth, remodeling, and adaptation: theory and numerical verification. Int J Numer Method Biomed Eng 29(8):822–49

Vorp DA, Geest JP Vande (2005) Biomechanical determinants of abdominal aortic aneurysm rupture. Arterioscler Thromb Vasc Biol 25(8):1558–1566

Vorp DA, Lee PC, Wang DHJ, Makaroun MS, Nemoto EM, Ogawa S, Webster MW (2001) Association of intraluminal thrombus in abdominal aortic aneurysm with local hypoxia and wall weakening. J Vasc Surg 34(2):291–99

Watton PN, Hill NA (2009) Evolving mechanical properties of a model of abdominal aortic aneurysm. Biomech Model Mechanobiol 8(1):25–42

Watton PN, Hill NA, Heil M (2004) A mathematical model for the growth of the abdominal aortic aneurysm. Biomech Model Mechanobiol 3(2):98–113

Watton PN, Raberger NB, Holzapfel GA, Ventikos Y (2009) Coupling the hemodynamic environment to the evolution of cerebral aneurysms: computational framework and numerical examples. J Biomech Eng 131(10):10. https://doi.org/10.1115/1.3192141

Wilson JS, Baek S, Humphrey JD (2013) Parametric study of effects of collagen turnover on the natural history of abdominal aortic aneurysms. Proc R Soc A 469(2150):20120556

Zeinali-Davarani S, Baek S (2012) Medical image-based simulation of abdominal aortic aneurysm growth. Mech Res Commun 42:107–17

Zeinali-Davarani S, Sheidaei A, Baek S (2011) A finite element model of stress-mediated vascular adaptation: application to abdominal aortic aneurysms. Comput Methods Biomech Biomed Eng 14(9):803–17

Zhou X, Raghavan ML, Harbaugh RE, Lu J (2010) Specific wall stress analysis in cerebral aneurysms using inverse shell model. Ann Biomed Eng 38(2):478–89